Adv. Elec. Mater. (2017) DOI: 10.1002/aelm.201600376

$Tm_3Fe_5O_{12}$/Pt Heterostructures with Perpendicular Magnetic Anisotropy for Spintronic Applications

Andy Quindeau[*1], Can O. Avci[1], Wenqing Liu[2,3], Congli Sun[4], Maxwell Mann[1], Astera T. Tang[1], Mehmet C. Onbasli[1], David Bono[1], Paul M. Voyles[4], Yongbing Xu[2], Jason Robinson[3], Geoffrey S. D. Beach[1] and Caroline A. Ross*[*1]*

[1]Department of Materials Science and Engineering, Massachusetts Institute of Technology, Cambridge, Massachusetts 02139, USA

[2]Department of Electronics, University of York, York YO10 5DD, UK

[3]Department of Materials Science and Metallurgy, University of Cambridge, 27 Charles Babbage Road, Cambridge CB3 0FS, UK

[4]Department of Materials Science and Engineering, University of Wisconsin-Madison, Madison, Wisconsin 53706, USA

* Correspondence: caross@mit.edu and quindeau@mit.edu

Abstract With recent developments in the field of spintronics, ferromagnetic insulator (FMI) thin films have emerged as an important component of spintronic devices. Yttrium iron garnet in particular is an excellent candidate for spin logic applications due to its low magnon damping and large spin wave propagation length. However, it has been a challenge to find FMI thin films with perpendicular magnetic anisotropy (PMA) which share these characteristics. Such materials could enable the development of low dissipation memory and logic devices based on spin orbit torques. In this work, we demonstrate robust PMA in strained ultra thin thulium iron garnet (TmIG) films of high structural quality down to a thickness of 5.6 nm which retain a magnetization close to bulk. Platinum deposited on TmIG possesses large spin Hall magnetoresistance (SMR), which indicates efficient spin transmission across the TmIG/Pt interface, and SMR measurements are used to characterize the magnetic anisotropy of the TmIG.

1. Introduction

Harnessing the electron's second fundamental property, its spin, is the basis of spintronic phenomena and devices.[1] These include recently discovered phenomena such as the quantum anomalous Hall effect[2] in magnetic topological insula- tors (TIs),[3] spin transfer torque[4,5] effects in nonmagnetic metal/ferromagnetic metal/oxide heterostructures, and spin orbit torque (SOT) effects in heterostructures that include ferro- magnetic metals/heavy metals,[6–8] magnetically-doped TIs,[6–8] and FMI/heavy metals where the FMI is a garnet[9] or Ba hexaferrite.[10] To realize novel circuit devices based on these effects a variety of magnetic materials and heterostructures has still to be developed in which the magnetic properties and interfacial spin transport can be controlled.

FMIs with PMA are of particular interest in spintronics. In FMI/heavy metal or FMI/TI heterostructures, current is lim- ited to the metal or to the surface layer of the TI which reduces the conductivity (and potentially the power consumption) com- pared to all-metallic structures, and avoids the possibility of direct spin transfer torque from current flow in the FMI layer. This facilitates the study of proximity effects, SOT and other exotic phenomena occurring at the interfaces, enabling for ex- ample an identification of the various contributions to spin orbit torques. Moreover, the presence of PMA in the FMI leads to stray-field-induced interface effects even at remanence. Do- main walls in PMA films also have qualitatively different struc- tures and dynamics compared to those of FMIs with in-plane magnetic anisotropy, which is relevant to racetrack memory or logic devices. Thus there is considerable interest in developing PMA FMI materials and heterostructures.

One of the most prominent classes of FMI is that of ferrimagnetic iron garnets, of which the best studied is $Y_3Fe_5O_{12}$ (YIG). The ultralow damping[11] and magneto-optical properties[12,13] of YIG are well known. The former makes YIG a suitable candidate for spin wave logic[14] and signal transmitters[15] due to the extremely large magnon propaga- tion length of several tens of millimeters. YIG/heavy metal (e.g., Pt, W, Ta) and YIG/topological insulator heterostructures have demonstrated proximity effects, spin pumping, spin See- beck, and other spintronic phenomena.[15–19] However, YIG films generally have an in-plane easy axis dominated by shape anisotropy due to the weak

magnetocrystalline anisotropy and magnetostriction of YIG. Epitaxial[20] and polycrystalline[21,22] YIG films have been reported to show PMA at low thickness as a result of magnetoelastic anisotropy arising from lattice mismatch and thermal mismatch respectively, but the fabri- cation of good quality YIG films with high out-of-plane remanence remains elusive. Fortunately, the magnetic properties of iron garnets can be dramatically altered by substitution of rare earths onto the Y sites. Kubota et al.[23, 24] showed that 50 nm thick thulium iron garnet ($Tm_3Fe_5O_{12}$, TmIG) possesses PMA caused by magnetoelastic anisotropy[25] when grown epitaxially on (111)-oriented gallium gadolinium garnet ($Gd_3 Ga_5 O_{12}$ or GGG), and we recently demonstrated[9] reversible magnetiza- tion switching via SOT in an 8 nm thick TmIG film grown on GGG, coated with Pt and patterned into a Hall cross.

In the present article, we provide a comprehensive descrip- tion of the structural characteristics and magnetic properties of thin films of TmIG with thickness of 5.6–30 nm grown on GGG, as well as the electrical properties of TmIG/Pt het- erostructures. The TmIG films show bulk magnetization, mod- erate coercivity (≈30 mT), high out-of-plane remanence, and a ferrimagnetic structure with compensation point below 1.5 K. We demonstrate that efficient spin transport can be achieved through the TmIG/Pt interface by measuring spin Hall magne- toresistance (SMR) in Pt, which leads to a large AHE signal in the Pt heavy metal layer. Lastly, we use the strong SMR signal to measure the anisotropy field of the TmIG film electrically, which is inaccessible by conventional magnetometry measure- ments due to the dominant paramagnetic contribution of the GGG substrate. We identified the magnetoelastic and magne- tocrystalline contributions to the total magnetic anisotropy, and we show that the spin mixing conductance is invariant in a tem- perature regime at and above room temperature. The TmIG/Pt heterostructure is thereby shown to be a robust system for further investigation of interfacial spintronic phenomena in a PMA FMI.

2. Structural Characterization of TmIG/GGG

Several TmIG films of thickness 5.6–30 nm were grown on (111)-oriented GGG by pulsed laser deposition as described in the Experimental Section. The results of structural characterization of the TmIG films are summarized in **Figure 1**. Thickness was determined by X-ray reflectometry (XRR) scans (not shown), and yielded a thickness of 5.6 nm (0.1 nm) for

the thinnest film examined.

2.1. Temperature Dependent Strain of TmIG/GGG

Garnets crystallize in the cubic structure with lattice parameter around 1.2 nm and eight formula units in the unit cell. GGG has an excellent lattice match with YIG and other iron garnets, and as expected, TmIG grew epitaxially on GGG substrates. Fig- ure 1a shows the symmetric high resolution X-ray diffraction (XRD) scan of a 19.7 nm thick TmIG film on GGG, revealing only (*hhh*)-type reflections, and yielding an out-of-plane lattice spacing of $d^{\mathrm{TmIG,\ XRD}}{}_{444}$ = 0.1769 nm. Laue fringes around the TmIG peak indicate the high crystalline quality and thickness uniformity of the layer. (Peaks from thinner films could not be resolved using XRD.)

A reciprocal space map of the 19.7 nm thick TmIG film around the TmIG and GGG (624)+ asymmetric peaks (Fig- ure 1b) confirms the coherent growth of the TmIG on the GGG substrate. The in-plane values for the (220) lattice spac- ing for both the TmIG film and the substrate are $d^{\mathrm{TmIG}}{}_{220} = d_{220}{}^{\mathrm{GGG}} = q_x{}^{-1}$ = 0.4377 nm, i.e., the cubic lattice parameter a = 1.238 nm which is in very good agreement with literature val- ues for GGG.[26] The out-of-plane lattice spacing for the TmIG film according to RSM is $d^{\mathrm{TmIG,\ RSM}}{}_{444} = q_z{}^{-1}$ = 0.1768 nm, very close to that measured by symmetric XRD. The differences be- tween the in-plane and out-of-plane lattice spacing of (111) TmIG show that the TmIG unit cell is compressively strained in the [111] out-of-plane direction due to its epitaxy with the GGG. The resulting distortion angle for the facets of the TmIG unit cell is β = 90.77 (Figure 1c,d). We assume that, since the 19.7 nm thick film is fully strained to the substrate, thinner films are also fully strained.

Temperature-dependent measurements of the d_{444} lattice parameter of GGG, the pseudo-cubic d_{444} of TmIG (calculated as the cube root of the unit cell volume) and the distortion angle β are shown in Figure 1c for the temperature range of 50–200 °C. The data yield linear thermal expansion coefficients in the (111) direction of $\mathrm{L,\ GGG} = 14.1 \times 10^{-6}\ \mathrm{K}^{-1}$ and $\mathrm{L,\ TmIG} = 15.57 \times 10^{-6}\ \mathrm{K}^{-1}$ for the substrate and the film, respectively. Evidently, the lattice mismatch strain decreases slowly with increasing temperature.

2.2. Surface Morphology and Crystal Quality

The surface morphology of the 19.7 nm thin TmIG film was measured via atomic force microscopy and exhibits an RMS roughness value of 1.5 nm calculated from the topographic image (**Figure 2**a). This film showed a few particles which led to the high roughness, but the roughness of the thinner films used for electrical studies was as low as 0.2 nm.

The crystal quality and interface structure were examined using high resolution scanning transmission electron mi- croscopy (STEM) of a cross-section of a TmIG/GGG sample. An image taken along the [$11\bar{2}$] direction is shown in Figure 1e. The yellow arrow indicates the interface between the TmIG and the GGG substrate. There is no evidence of dislocations in the crystal structure of TmIG or at the interface over the field of the images. Figure 1f shows a high angle annular dark field scanning transmission electron microscopy (HAADF-STEM) image in the [101] direction and corresponding electron energy loss spectroscopy (EELS) line scans (Figure 1f) perpendicular to the interface, which show Tm and Fe in the film and Ga and Gd in the substrate, indicating little or no interdiffusion of the cations between the garnet materials.

3. Magnetic Characterization

3.1. Hysteresis and Domain Structure

Polar magneto-optical Kerr effect (MOKE) and vibrating sam- ple magnetometry (VSM) measurements on the 5.6 nm thin TmIG film are shown in Figure 2c,d. These both reveal the hysteresis loop shape and coercivity but only the VSM gives a quantitative measurement of magnetic moment; however, the paramagnetic background of the GGG substrate impedes measurements of hysteresis loops by VSM. The films exhibit a square hysteresis loop with coercivity of 23.9 kA m^{-1}. No hysteretic behavior was measurable for an in-plane loop, which indicates uniaxial anisotropy with easy axis along the surface normal. Based on the thickness derived from an XRR mea- surement, the saturation magnetization M_S for the 5.6 nm thick TmIG sample and the Pt/TmIG(8 nm) sample was 100 (±1.5) kA m^1, and several other films of different thickness gave values of 90–100 kA m^1. This is in good agreement with data measured for bulk TmIG.[25]

Measurements of magnetic damping of the TmIG films were challenging due to the very low signal to noise ratio and the PMA, but gave values in the range of $\alpha \sim 10^{-3}$ for a TmIG film on (100) GGG which exhibited in-plane magnetization. Prior work on bulk TmIG showed an FMR line width of H = 5.17 kA m^1[27] which is one of the lower values reported for a range of rare earth garnets.[28]

Magnetic force microscopy (MFM) was used to image the domain structure of the thicker films. Figure 2b shows an MFM image of the 19.7 nm thin TmIG film after demagneti- zation, performed by placing the sample in a 10 Hz alternating magnetic field whose amplitude decreased approximately ex- ponentially from 160 to 0 kA m^1 over a time period of 2 min. The domain pattern is typical for PMA materials without lateral anisotropy[29] with a period of ≈0.3 μm, and the area coverage of up- and down-magnetized domains is, as expected, approxi- mately equal.

3.2. Determination of the Magnetic Anisotropy

The magnetic anisotropy of the TmIG films includes contri- butions from magnetocrystalline, magnetoelastic, and shape anisotropies. Room temperature values for the first order cubic anisotropy constant K_1 and the magnetostriction coefficients λ_{111} and λ_{100} of bulk TmIG have been reported to be −1.1 kJ m^3 < K_1 < − 0.58 kJm^3, $\lambda_{111} = -5.2 \times 10^6$ and $\lambda_{001} = 1.4 \times 10^6$.[25] The uniaxial anisotropy K_u is the difference between the total magnetic energy when the magnetization is oriented in-plane versus out of-plane, and can be written as[30]

$$K_u = E_{IP} - E_{OP} = -{}^{K_1}/_{12} + {}^{9}/_{8}\lambda_{111}c_{44}\left({}^{\pi}/_{2} - \beta\right) - \left({}^{\mu_0}/_{2}\right)M_S{}^{2}\ [22]. \qquad \textbf{(1)}$$

In this expression the magnetocrystalline anisotropy is $-\ {}^{K}\ {}^{1}/_{12}$, the magnetoelastic anisotropy is ${}^{9}/_{8}8111\ c\ 44\ ({}^{B}/_{2}-\ \beta)$, and the shape anisotropy is $-(\mu_0/2)\ M\ {}^{2}$. The magnetoelastic term is proportional to both the magnetostriction coefficient λ_{111} and to the shear strain which is related to the distortion angle β. The shear modulus is c_{44} = 76.4 GPa[31] for YIG at room temperature, and 74–90 GPa for rare earth iron garnets. The magnetocrystalline anisotropy is the smallest contribution to K_u, and the magnetoelastic

anisotropy competes with and overcomes the shape anisotropy.

3.3. Element-Specific Ferrimagnetic Configuration

X-ray magnetic circular dichroism (XMCD) measurements were carried out to determine the relative orientations of the magnetic moments of the Tm^{3+} and Fe^{3+} cations. XMCD is derived from X-ray absorption spectra (XAS) which clearly show a helicity-dependent X-ray absorption (Figure 2e,f, upper panels).The XMCD signal is calculated as

$I_{asy} = \frac{I_{\sigma-} - I_{\sigma+}}{I_{\sigma-} + I_{\sigma+}}$, where I is the total electron yield (TEY)-XAS intensities for the respective helicities of the emitted light (Figure 2e,f, lower panels).

The XMCD spectra around the Fe $L_{2,3}$ edges are consistent with antiferromagnetic coupling between Fe in the a-sites (oc- tahedral, two per formula unit) and d-sites (tetrahedral, three per formula unit) sites in the garnet unit cell, as expected for iron garnets. The spectra around the $M_{4,5}$ edges of Tm confirm that the Tm^{3+} ions are magnetized antiparallel to the a-site Fe^{3+} ions.[32] This agrees with the fact that the d-site Fe^{3+} peak is at lower photon energy than the a-site Fe^{3+} peak, similar to the general case of iron spinels.[33, 34] The spectral shape of the core spectra are characteristic of the Tm^{3+} $4f^{12}$ configuration.[35]

Our temperature-dependent XMCD measurements (not shown here) indicated that no compensation point was present for the TmIG thin films in the temperature range between 1.5 and 300 K, i.e., the net magnetization remains parallel to the tetrahedral Fe^{3+}. The existence of a compensation temperature in bulk TmIG has not been confirmed.[36, 37]

4. Spintronic Interface Properties of TmIG/Pt Heterostructures

4.1. Anomalous Hall Effect

We use electrical measurements in GGG/TmIG(8 nm)/Pt(5 nm) heterostructures to access the spin mixing properties of the TmIG/Pt interface as well as measuring the PMA of TmIG. Pt is well suited to convert charge current into a pure spin current and vice versa by virtue of its

large spin-orbit coupling combined with low resistivity. Recently, it has been discovered that Pt in contact with an FMI can show magnetoresistance due to the interaction of the spin Hall effect-induced spin accumulation at the Pt/FMI interface with the magnetization (**m**) of a FMI.[38] This so-called SMR increases (decreases) the longitudinal resistance when the spin current is absorbed (reflected) by the FMI.

The spin current transmission across interfaces is dictated by the spin mixing conductance concept, which parameterizes the interface transparency to the spin current, and is crucial for SMR,[16, 39] spin Seebeck effect,[40] and spin-orbit torque[41] stud- ies. The additional SMR contribution to the longitudinal resis- tance scales with $R\ \mathbf{m}^2{}_{\mathbf{y}}$ assuming charge current flow along x, with z being the direction normal to the layer plane. The SMR also has a transverse (Hall resistance) component with symme- try $R_{\mathrm{SMR}}\ \mathbf{m_x}\ \mathbf{m_y}$ analogous to the planar Hall effect in ferromag- nets. Additionally, it has been theorized[42] and measured[17] that the imaginary part of the spin mixing conductance gives rise to a transverse anomalous Hall-like signal with symmetry $R_{\mathrm{AHE}}\ \mathbf{m_z}$ that has much lower amplitude compared to R_{SMR} . By combining these and the ordinary Hall effect of Pt we can write the expected angular symmetry of the transverse Hall effect resistance (R_H) as follows

$$R_H = R_{SMR}\sin^2 2\sin 2n + R_{AHE}\cos 2 + R_{OHE}\,H_z \quad (2)$$

where θ and φ are the polar and azimuthal angles of $\boldsymbol{m}$, respectively, as depicted in Fig.3a, and R_{OHE} is the ordinary Hall resistance due to an out-of-plane field H_z.

To characterize the SMR, anomalous Hall effect and ordi- nary Hall effect (OHE) in 5 nm Pt/8 nm TmIG bilayers we injected an ac current of root mean square amplitude I_{ac} = 1.8 mA with frequency $\omega/2\pi$ = 3678 Hz, and measured the first harmonic Hall voltage as shown schematically in Figure 3a. This is equivalent to standard dc measurements but with much higher signal-to-noise ratio. The inset shows the optical microscope image of the device utilized for electrical measure- ments. Figure 3b depicts the Hall resistance for an out-of-plane field sweep. We recognize the AHE contribution following $\mathbf{m_z}$ which reverses between up and down states at the coercive field of ≈ 11.9 KA m^{-1} . The linear slope independent of **m** direction (orange dashed lines) gives R_{OHE}. This measurement shows that

m has 100% remanence, and sharp transitions between up and down states suggest low pinning and efficient propa gation of domain walls, assuming that the reversal is mediated by domain nucleation and propagation.

To determine the spin mixing conductance at the TmIG/Pt interface, we measure R_H for different in-plane angles φ when the film is saturated in plane. Figure 3d shows R_H obtained at $H = \pm 318.3$ KAm^{-1} versus φ. We fit the data by using Equation (2) and obtain $R_{SMR} = 8.2$ m . By transforming R_{SMR} and R into resistivity, taking D $^{Pt} = 40$: cm as measured AHE $_{xx}$ on the same device, assuming $\theta_{SH} = 0.08$ for Pt and taking he spin diffusion length to be $\lambda_{Pt} = 1.4$ nm, we calculate the real and imaginary part of the spin mixing conductance as $G^{\uparrow\downarrow} = 1.3 \times 10^{14}$ $^{-1}$m^{-2} and $G^{\uparrow\downarrow} = 4.8 \times 10^{12}$ $^{-1}$m^{-2}, respectively. These values are close to the ones reported for Pt/YIG[16,17] and our measurement on another Pt/TmIG device[9] and suggest highly efficient transmission of spin cur- rent across the Pt/TmIG interface.

4.2. Measurement of the Total Magnetic Anisotropy

Figure 3c exhibits R_H for in-plane field sweeps at various φ. In this geometry R_{OHE} does not contribute to the signal, and thus we can characterize R_{SMR} by analyzing the angular dependence of the signal at high fields where **m** tilts in-plane thus R_{AHE} be- comes negligibly small. The specific U-shape of the signal is due to coherent rotation of the magnetization toward the film plane at higher H. We find that $H \geq 199$ KA m^{-1} is necessary to saturate **m** fully in-plane, which gives an indication of the ef- fective perpendicular magnetic anisotropy field (H_K) of TmIG. Macrospin simulations[9] suggest that for this measurement H_K $^{\sim}$=198.9 ± 15.9 KA m^{-1} .

The features around $H = 0$ KA m^{-1} are due to R_{AHE} since **m** switches between up and down states due to a small uninten- tional out-of-plane component of the field. With the values for H_K and M_S, the total anisotropy energy at room temperature was calculated to be $K_u = 11.88$ kJ m^{-3} . The contribution from shape anisotropy is well known, but the measurement cannot separately identify the contributions of magnetocrystalline and

magnetoelastic anisotropies. However, based on the estimate of K_1 from the literature, magnetocrystalline anisotropy is the dominant contribution to producing PMA in the TmIG film. From the negative sign of λ_{111} and the out-of-plane compressive strain state in the film, the magnetoelastic anisotropy favors an out-of-plane easy axis so K_{ME} is positive, with magnitude $\approx$17.5 kJm^{-3}.

4.3. The Effect of Joule Heating on Magnetic Anisotropy

We now discuss the effect of temperature rise due to Joule heat- ing on H_K. Figure 3e shows R_H measured at $\varphi_H = +\pi/4$ with applied current varying between 1.8 and 10.2 mA, correspond- ing to $j = 4.8 \times 10^{10}$ and 2.72×10^{11} KA m^{-2} , respectively. We observe that, although the SMR amplitude remains nearly the same, the field required to saturate **m** fully in-plane decreases systematically, as well as the coercivity. We attribute this behav- ior to H_K decreasing as a function of increasing temperature due to Joule heating rather than to changes in the M_S. In Fig- ure 3f we plot H_K as a function of I_{app} (purple squares). When I_{app} is increased from 1.8 to 10.2 mA, H_K decreases more than 50%.

To further support the hypothesis that heating lowers H_K, we measure the device resistance as a function of I_{app} and inde- pendently measure the device resistance for low I_{app}(i.e., with minimum Joule heating) at different temperatures by placing the device in a heated environment. By correlating these two measurements we can determine the actual changes in the de- vice temperature (T_{device}) as a function of I_{app} (Figure 3f right axis). At 10 mA the temperature is 85 $^\circ$ C (i.e., the temperature increase was 65 $^\circ$C above ambient). From the XRD data, this corresponds to a lattice distortion angle of 90.75°, compared to 90.77° at room temperature (Figure 1c). The small change in strain between RT and 85 $^\circ$C, and the dominant magne- toelastic contribution to K_u, suggest that the change in H_K is not caused by a change in the magnetocrystalline anisotropy. Instead, we believe the significant fall in H_K due to heating is primarily governed by a strong temperature dependence of the magnetoelastic anisotropy.

The net PMA was confirmed by magnetometry measure- ments on partly strain-relaxed TmIG films grown on (111)- oriented GGG substrates. These films were grown then

im- mediately annealed for 3 h at the deposition temperature and pressure. XRD scans (not shown) indicated closer to bulk values of the out-of-plane lattice parameters in the films. Despite this, magnetometry measurements showed that the films still exhib- ited PMA. This shows that PMA could be present even in partly strain-relaxed films with a smaller magnetoelastic anisotropy.

5. Conclusion

In summary, we characterized thin film ferrimagnetic garnet TmIG grown epitaxially on GGG that possesses high structural quality and robust perpendicular magnetic anisotropy down to a thickness of 5.6 nm. We showed strong spin mixing conduc- tance at the interface between Pt and TmIG, which led to a large AHE signal in the Pt layer and enabled electrical measurement of the magnetic state of the TmIG. By exploiting the SMR of the TmIG/Pt bilayer, we directly measured the anisotropy field of the TmIG and its temperature dependence due to Joule heat- ing. The PMA is mainly a result of magnetoelastic anisotropy with a contribution from magnetocrystalline anisotropy.

We propose that the high spin mixing conductance and perpendicular anisotropy found in TmIG/Pt heterostructures are promising attributes for future studies of a range of spin- tronic heterostructures such as FMI/topological insulators and phenomena such as quantum anomalous Hall and proximity effects. This emphasizes the value of TmIG for spintronic ex- periments that require FMI layers with PMA.

6. Experimental Section

Fabrication of the Thin Films: TmIG thin films were deposited using PLD on single-crystal GGG substrates with (111) orien- tation. The stoichiometric target used during the deposition process was made in house by mixing powders of Tm and Fe oxides in the appropriate weight ratios, and then calcining the mix at 1150 $^{\circ}$C for 5 h, cold-pressing it into a target, and sin- tering the target at 1350 $^{\circ}$C for 10 h. The stoichiometry of the target was confirmed by wavelength dispersion spectroscopy conducted at various locations on the target surface. To ensure epitaxial growth conditions during the PLD process, a substrate temperature of 650 $^{\circ}$C, a laser fluence of 2 J cm^{-2}, a laser rep- etition rate of 10 Hz, and an O_2 pressure of 200 mTorr were applied. After the deposition the substrate was cooled down to room temperature

in 200mTorr O_2 at a rate of 2 $Kmin^{-1}$. It was found that an additional annealing step was not necessary, but the slow cooling step after deposition was crucial in order to obtain the best quality films.

Transmission Electron Microscopy: Cross-sectional TEM imaging of the structure was carried out using a FEI TITAN (S)TEM with a CEOS probe aberration corrector operated at 200 KV, which achieves a spatial resolution of less than 0.8 A°. The use of a HAADF detector in STEM mode allowed the authors to record elastic, thermal diffuse scattering events that are proportional to Z^2 and thus determine the position of atom columns or individual atoms as brightness contrast propor- tional to their atomic number. The TEM lamellas were prepared using a focused ion beam (Zeiss Auriga cross beam system).

Synchrotron Study: A detailed investigation of the element- specific magnetic structure of TmIG was conducted on a 19.7 nm thin sample using XMCD at the Diamond Light Source, UK. XAS were collected at the Tm $M_{4,\,5}$ and Fe $L_{2,\,3}$ absorption edges by TEY measurements, assisted by an ultrathin (3 nm) Au capping layer on top of the TmIG. Oppositely circular polarized X-rays with 100% degree of polarization were used successively to resolve XMCD signals from the respective elements. The light-helicity was switched in a saturating magnetic field of 6 T, which was applied normal to the film plane and in parallel with the incident beam.

Hall Cross Fabrication: To study the properties of TmIG as a spinterface material, the authors sputtered 5 nm Pt on top of an 8 nm thin TmIG film. The authors then defined 16 × 7 μm^2 sized Hall crosses in resist by a photolithography process and used ion milling to create Pt/TmIG mesa structures. Using etching instead of a liftoff process improved the quality of the Pt/TmIG interface by avoiding residual resist layers between the TmIG and the Pt.

Acknowledgements

The authors acknowledge support from C-SPIN, one of the six SRC STARnet Centers sponsored by MARCO and DARPA. A.Q. acknowledges funding from the Max Planck Society and the Deutsche Forschungsgemeinschaft (DFG, German Re- search Foundation).

References

[1] C. Chappert, A. Fert, F. N. Van Dau, *Nat. Mater.* **2007**, *6*, 813.

[2] C.-Z. Chang, J. Zhang, X. Feng, J. Shen, Z. Zhang, M. Guo, K. Li, Y. Ou, P. Wei, L.-L. Wang, Z.-Q. Ji, Y. Feng, S. Ji, X. Chen, J. Jia, X. Dai, Z. Fang, S.-C. Zhang, K. He, Y. Wang, L. Lu, X.-C. Ma, Q.-K. Xue, *Science* **2013**, *340*, 167.

[3] Y. Ando, *J. Phys. Soc. Jpn.* **2013**, *82*, DOI 10.7566/JPSJ.82.102001.

[4] J. C. C. Slonczewski, *J. Magn. Magn. Mater.* **1996**, *159*, DOI 10.1016/0304-8853(96)00062-5.

[5] L. Berger, *Phys. Rev. B* **1996**, *54*, 9353.

[6] I. M. Miron, K. Garello, G. Gaudin, P. J. Zermatten, M. V. Costache, S. Auffret, S. Bandiera, B. Rodmacq, A. Schuhl, P. Gambardella, *Nature* **2011**, *476*, 189.

[7] L. Q. Liu, C.-F. Pai, Y. Li, H. W. Tseng, D. C. Ralph, R. A. Buhrman, *Science* **2012**, *336*, 555.

[8] Y. Fan, P. Upadhyaya, X. Kou, M. Lang, S. Takei, Z. Wang, J. Tang, L. He, L. Chang, M. Montazeri, G. Yu, W. Jiang, T. Nie, R. N. Schwartz, Y. Tserkovnyak, K. L. Wang, *Nat. Mater.* **2014**, *13*, 699.

[9] C. O. Avci, A. Quindeau, C.-F. Pai, M. Mann, L. Caretta, A. S. Tang, M. C. Onbasli, C. A. Ross, G. S. D. Beach, unpublished.

[10] P. Li, T. Liu, H. Chang, A. Kalitsov, W. Zhang, G. Csaba, W. Li, D. Richardson, A. DeMann, G. Rimal, H. Dey, J. S. Jiang, W. Porod, S. B. Field, J. Tang, M. C. Marconi, A. Hoffmann, O. Mryasov, M. Wu, *Nat. Commun.* **2016**, *7*, 12688.

[11] C. Hauser, T. Richter, N. Homonnay, C. Eisenschmidt, H. Deniz, D. Hesse, S. Ebbinghaus, G. Schmidt, N. Weinberg, *Sci. Rep.* **2016**, *6*, DOI 10.1038/srep20827.

[12] Y. Shoji, T. Mizumoto, H. Yokoi, I. W. Hsieh, R. M. Osgood, *Appl. Phys. Lett.* **2008**, *92*.

[13] B. J. H. Stadler, T. Mizumoto, *IEEE Photonics J.* **2014**, *6*.

[14] T. Schneider, A. A. Serga, B. Leven, B. Hillebrands, R. L. Stamps, M. P. Kostylev, *Appl. Phys. Lett.* **2008**, *92*.

[15] Y. Kajiwara, K. Harii, S. Takahashi, J. Ohe, K. Uchida, M. Mizuguchi, H. Umezawa, H. Kawai, K. Ando, K. Takanashi, S. Maekawa, E. Saitoh, *Nature* **2010**, *464*, 262.

[16] N. Vlietstra, J. Shan, V. Castel, B. J. van Wees, J. Ben Youssef, *Phys. Rev. B* **2013**, *87* , 184421.

[17] S. Meyer, R. Schlitz, S. Geprags, M. Opel, H. Huebl, R. Gross, S. T. B. Goennenwein, *Appl. Phys. Lett.* **2015**, *106*, 132402.

[18] M. Schreier, N. Roschewsky, E. Dobler, S. Meyer, H. Huebl, R. Gross, S. T. B. Goennenwein, *Appl. Phys. Lett.* **2013**, *103*, 242404.

[19] A. Hamadeh, O. D. Kelly, C. Hahn, H. Meley, R. Bernard, A. H. Molpeceres, V. V Naletov, M. Viret, A. Anane, V. Cros, S. O. Demokritov, J. L. Prieto, M. Munoz, G. de Loubens, O. Klein, *Phys. Rev. Lett.* **2014**, *113*, 197203.

[20] H. Wang, C. Du, P. C. Hammel, F. Yang, *Phys. Rev. B* **2014**, *89*, 134404.

[21] E. Popova, N. Keller, F. Gendron, M. Guyot, M. C. Brianso, Y. Dumond, M. Tessier, *J. Appl. Phys.* **2001**, *90*, 1422.

[22] E. Popova, N. Keller, F. Gendron, L. Thomas, M.-C. C. Brianso, M. Guyot, M. Tessier, S. S. P. Parkin, *J. Vac. Sci. Technol., A* **2001**, *19*, 2567.

[23] M. Kubota, A. Tsukazaki, F. Kagawa, K. Shibuya, Y. Tokunaga, M. Kawasaki, Y. Tokura, K. Shibuyay, Y. Tokunaga, M. Kawasaki, Y. Tokura, *Appl. Phys. Express* **2012**, *5*, 103002.

[24] M. Kubota, K. Shibuya, Y. Tokunaga, F. Kagawa, A. Tsukazaki, Y. Tokura, M. Kawasaki, *J. Magn. Magn. Mater.* **2013**, *339*, 63.

[25] A. Paoletti, *Physics Of Magnetic Garnets*, North-Holland Publish- ing Company, Amsterdam **1978**.

[26] H. Sawada, *J. Solid State Chem.* **1997**, *132*, 300.

[27] V. V. Randoshkin, V. I. Kozlov, Y. A. Koksharov, A. M. Saletskiĭ, N. N. Sysoev, N. N. Usmanov, *Tech. Phys.* **2007**, *52*, 495.

[28] V. J. Fratello, I. Mnushkina, S. J. Licht, R. R. Abbott, *Mater. Res. Soc. Symp. Proc.* **2005**, *834*.

[29] A. Hubert, R. Schäfer, in *Magnetic Domains*, Springer, New York **1998**, pp. 500–507.

[30] D. H. Kim, N. M. Aimon, L. Bi, J. M. Florez, G. F. Dionne, C. A. Ross, *J. Phys. Condens. Matter* **2013**, *25*, 26002.

[31] Y. A. Burenkov, S. P. Nikanorov, *Magn. Ferroelectr.* **2002**, *44*, 318.

[32] W. Meyer, W. Sturhahn, E. Gerdau, *Hyperfine Interact.* **1994**, *94*, 2059.

[33] W. Liu, L. He, Y. Zhou, K. Murata, M. C. Onbasli, C. A. Ross, Y. Jiang, Y. Wang, Y. Xu, R. Zhang, K. L. Wang, *AIP Adv.* **2016**, *6*, DOI 10.1063/1.4943157.

[34] W. Liu, L. He, Y. Xu, K. Murata, M. C. Onbasli, M. Lang, N. J. Maltby, S. Li, X. Wang, C. A. Ross, P. Bencok, G. van der Laan, R. Zhang, K. L. Wang, *Nano Lett.* **2015**, *15*, 764.

[35] B. T. Thole, G. van der Laan, J. C. Fuggle, G. A. Sawatzky, R. C. Karnatak, J.-M. Esteva, *Phys. Rev. B* **1985**, *32*, 5107

[36] S. Geller, J. P. Remeika, R. C. Sherwood, H. J. Williams, G. P. Espinosa, *Phys. Rev.* **1965**, *137* , 1034.

[37] R. L. Cohen, *Phys. Lett.* **1963**, *5*, 177.

[38] H. Nakayama, M. Althammer, Y. T. Chen, K. Uchida, Y. Kajiwara, D. Kikuchi, T. Ohtani, S. Geprags, M. Opel, S. Takahashi, R. Gross, G. E. W. Bauer, S. T. B. Goennenwein, E. Saitoh, *Phys. Rev. Lett.* **2013**, *110*, 206601.

[39] M. Weiler, M. Althammer, M. Schreier, J. Lotze, M. Pernpeint- ner, S. Meyer, H. Huebl, R. Gross, A. Kamra, J. Xiao, Y. T. Chen, H. J. Jiao, G. E. W. Bauer, S. T. B. Goennenwein, *Phys. Rev. Lett.* **2013**, *111*, 176601.

[40] K. I. Uchida, H. Adachi, T. Ota, H. Nakayama, S. Maekawa, E. Saitoh, *Appl. Phys. Lett.* **2010**, *97*, 18.

[41] C. F. Pai, Y. X. Ou, L. H. Vilela-Leao, D. C. Ralph, R. A. Buhrman, *Phys. Rev. B* **2015**, *92*, 64426.

[42] Y. T. Chen, S. Takahashi, H. Nakayama, M. Althammer, S. T. B. Goennenwein, E. Saitoh, G. E. W. Bauer, *Phys. Rev. B* **2013**, *87* , 144411.

Figures

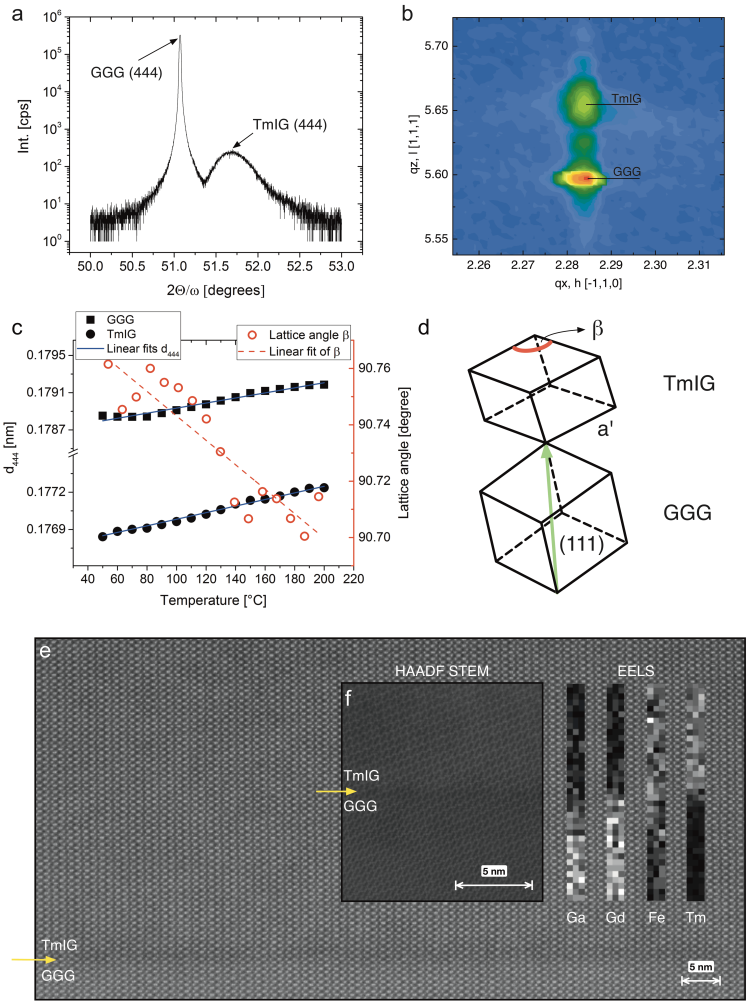

Figure 1 - Structural characterization of TmIG. a), XRD symmetric scan of the TmIG(19.7 nm)/GGG sample around the (444) peak. b), Reciprocal space map of the asymmetric $(624)_+$ diffraction peaks of the substrate GGG (lower peak) and the film (upper peak). c) Temperature evolution of the TmIG and GGG d_{444} lattice parameters and of the resulting lattice distortion angle β. d), Sketch of the two adjacent unit cells of TmIG and GGG at the interface. The deformation of the pseudocubic TmIG unit cell is exaggerated. e)+f) HAADF STEM images of the TmIG/GGG structure at the interface in (e) the $[10\bar{2}]$- direction and (f) the $[10\bar{2}]$- direction. EELS line scans at the interface show the distribution of Ga, Gd, Fe, and Tm atoms as black-white contrast.

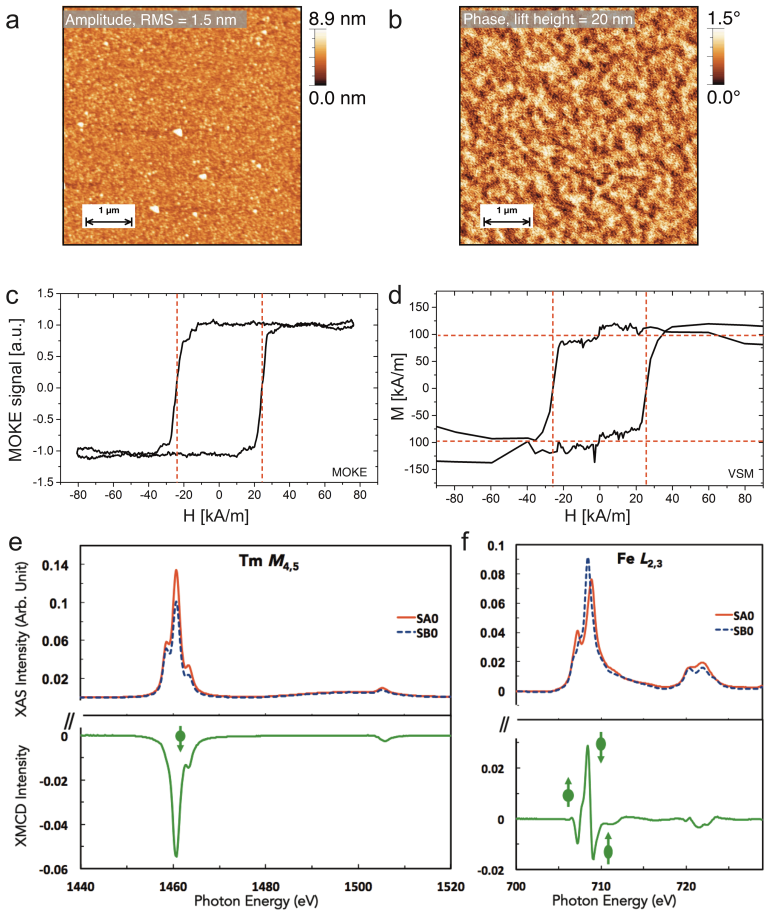

Figure 2 - Magnetic characterization of TmIG thin films. (a) Amplitude- and (b) phase images of a MFM scan on the TmIG thin film. The RMS surface roughness is 1.5 nm and characteristic stripe domains possess a feature size ~ 1 µm. (c), Polar MOKE signal versus applied out-of-plane magnetic field for the 5.6 nm thick TmIG film. (d), Vibrating sample magnetometer measurement on the same film with field applied normal to the sample plane. (e,f) The XAS (upper panel) and XMCD (lower panel) asymmetric intensity signals for (e) the $M_{4,5}$ edge of Tm and (f) the $L_{2,3}$ edge of Fe. The arrows in the lower figures correspond to the magnetization direction at the respective energy peak, pointing up (down) for positive (negative) XMCD signal.

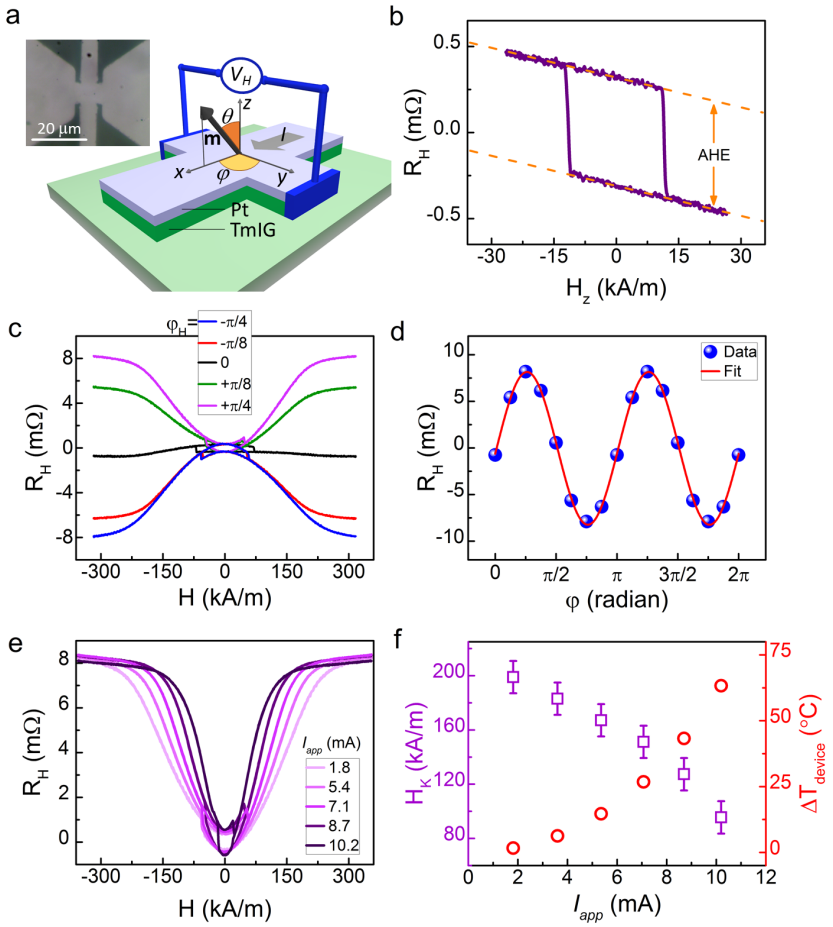

Figure 3 - SMR measurements on a TmIG/Pt bilayer device. a), Schematics of the electrical measurements and the definition of coordinate axes and angles. Upper left: optical image of the measured device. b), Hall resistance as a function of the out-of-plane field showing the anomalous Hall (two levels) and ordinary Hall (linear slope) contributions. c), Hall resistance as a function of an in-plane field sweep applied at different angles φ. d), In-plane angular variation of the Hall resistance recorded at $H = \pm 318\ {}^{\mathrm{kA}}/_{\mathrm{m}}$. Fit according to Eq.1 shows that the signal is purely driven by the SMR. e), Variation of Hall resistance as a function of applied current. Different shapes suggest that the effective anisotropy field depends on I_{app} and therefore on the Joule heating. f), Left axis: calculated PMA field and the variation of the device resistance as a function of I_{app}. We see that the increase of the resistance due to Joule heating correlates with the decrease in H_K. Right axis: Relative change in the device temperature as a function of applied current.